The Astrophysical Journal Letters, 918:L17 (7pp), 2021 September 1 https://doi.org/10.3847/2041-8213/ac1945

Elemental Abundances of the Hot Atmosphere of Luminous Infrared Galaxy Arp 299

Junjie Mao[1,2,3], Ping Zhou[4], Aurora Simionescu[3,5,6], Yuanyuan Su[7], Yasushi Fukazawa[8,9,10], Liyi Gu[3,11], Hiroki Akamatsu[3], Zhenlin Zhu[3,5], Jelle de Plaa[3], François Mernier[3,12], and Jelle S. Kaastra[3,5]
[1] Department of Physics, Hiroshima University, 1-3-1 Kagamiyama, HigashiHiroshima, Hiroshima 739-8526, Japan; jmao2018@hiroshima-u.ac.jp
[2] Department of Physics, University of Strathclyde, Glasgow G4 0NG, UK
[3] SRON Netherlands Institute for Space Research, Sorbonnelaan 2, 3584 CA Utrecht, The Netherlands
[4] School of Astronomy and Space Science, Nanjing University, Nanjing 210023, People's Republic of China
[5] Leiden Observatory, Leiden University, P.O. Box 9513, 2300 RA Leiden, The Netherlands
[6] Kavli Institute for the Physics and Mathematics of the Universe (WPI), The University of Tokyo, Kashiwa, Chiba 277-8583, Japan
[7] Department of Physics and Astronomy, University of Kentucky, 505 Rose Street, Lexington, KY, 40506, USA
[8] Department of Physical, Hiroshima University, 1-3-1 Kagamiyama, Higashi-Hiroshima, Hiroshima 739-8526, Japan
[9] Hiroshima Astrophysical Science Center, Hiroshima University, 1-3-1 Kagamiyama, Higashi-Hiroshima, Hiroshima 739-8526, Japan
[10] Core Research for Energetic Universe, Hiroshima University, 1-3-1 Kagamiyama, Higashi-Hiroshima, Hiroshima 739-8526, Japan
[11] RIKEN High Energy Astrophysics Laboratory, 2-1 Hirosawa, Wako, Saitama 351-0198, Japan
[12] European Space Agency (ESA), European Space Research and Technology Centre (ESTEC) Keplerlaan 1, 2201 AZ Noordwijk, The Netherlands
Received 2021 July 14; revised 2021 July 28; accepted 2021 July 29; published 2021 August 31

Abstract

Hot atmospheres of massive galaxies are enriched with metals. Elemental abundances measured in the X-ray band have been used to study the chemical enrichment of supernova remnants, elliptical galaxies, groups, and clusters of galaxies. Here we measure the elemental abundances of the hot atmosphere of luminous infrared galaxy Arp 299 observed with XMM-Newton. To measure the abundances in the hot atmosphere, we use a multi-temperature thermal plasma model, which provides a better fit to the Reflection Grating Spectrometer data. The observed Fe/O abundance ratio is subsolar, while those of Ne/O and Mg/O are slightly above solar. Core-collapse supernovae (SNcc) are the dominant metal factory of elements like O, Ne, and Mg. We find some deviations between the observed abundance patterns and theoretical ones from a simple chemical enrichment model. One possible explanation is that massive stars with $M_\star \gtrsim 23$–$27\,M_\odot$ might not explode as SNcc and enrich the hot atmosphere. This is in accordance with the missing massive SNcc progenitors problem, where very massive progenitors $M_\star \gtrsim 18\,M_\odot$ of SNcc have not been clearly detected. It is also possible that theoretical SNcc nucleosynthesis yields of Mg/O yields are underestimated.

Unified Astronomy Thesaurus concepts: Core-collapse supernovae (304); Chemical abundances (224); X-ray astronomy (1810); Starburst galaxies (1570); High resolution spectroscopy (2096); Galaxy groups (597); Interacting galaxies (802)

1. Introduction

Hot atmospheres of massive galaxies are enriched with metals (Werner et al. 2019). Metals are mainly produced by stars before and during their splendid death as supernovae (SN). Generally speaking, core-collapse supernovae (SNcc) of massive ($M_* \gtrsim 8\,M_\odot$) stars are the main metal factory of elements like O, Ne, and Mg (Nomoto et al. 2013). Type-Ia supernovae (SNIa) dominate the enrichment of the Fe-peak elements like Fe and Ni (Hitomi Collaboration et al. 2017). Low- and intermediate-massive stars ($M_* \lesssim 7\,M_\odot$) in the asymptotic giant branch (AGB) phase contribute most to light elements like N (Kobayashi et al. 2006; Werner et al. 2006; Mao et al. 2019).

In chemical enrichment models, it is common to assume that massive stars from $\sim 10\,M_\odot$ to $\gtrsim$40–50 $M_\odot$ can explode as SNcc and enrich the surrounding environment (e.g., Kobayashi et al. 2006; Sanders & Fabian 2006; de Plaa et al. 2007; Mernier et al. 2016; Mao et al. 2019). If the SNcc progenitor does not contain metals in its atmosphere (i.e., $Z_{\rm init} = 0$), very massive stars up to $M_* = 140\,M_\odot$ can also contribute to the chemical enrichment via SNcc (Nomoto et al. 2013). It is still debated whether very massive stars with higher initial metallicity could make successful SN explosions (Heger et al. 2003).

From the observational perspective, there is a missing massive SNcc progenitor problem as reviewed by Smartt (2015). Massive stars, especially those with $M_\star \gtrsim 18\,M_\odot$ might explode as a hypernova (HN), explode as a faint supernova ejecting a small amount of heavy elements, or directly form a black hole without a visible supernova (Nomoto et al. 2013). If the bulk of massive stars above a certain mass limit do not explode as SNcc or HN, we expect to see mismatches between the observed and theoretical abundance ratios.

Elemental abundances measured in the X-ray band have been used to decode the chemical enrichment of supernova remnants (e.g., Zhou & Vink 2018), elliptical galaxies, groups, and clusters of galaxies (e.g., Hitomi Collaboration et al. 2017; Mernier et al. 2018; Mao et al. 2019; Simionescu et al. 2019). Here, we present the elemental abundances of the hot atmosphere of a starburst galaxy, which form stars intensively.

Arp 299, also known as NGC 3690,[13] is a pair of interacting galaxies with a star formation rate of $119\,M_\odot\,{\rm yr}^{-1}$ (Smith et al. 2018) at the distance of 48.5 ± 3.4 Mpc (James et al. 2014). It is one of the most powerful nearby starburst galaxies (Alonso-Herrero et al. 2009). With $L_{\rm IR} = 6.3 \times 10^{14}\,L_\odot$ (Pereira-Santaella et al. 2011), it is qualified as a luminous infrared galaxy (Sanders & Mirabel 1996). From 1992 to 2010, seven

[13] IC 694 is a small elliptical or lenticular galaxy about an arcmin northwest, which is not part of Arp 299.

Table 1
XMM-Newton Observation Log

Date	ObsID	Effective Exposures
2001 May 6	0112810101	9.6 ks (RGS), 13.0 ks (pn)
2011 Dec 15	0679381101	9.8 ks (RGS), 6.4 ks (pn)
2020 May 8	0861250101	42.9 ks (RGS), 39.3 ks (pn)
2020 May 22	0861250201	34.9 ks (RGS), 26.3 ks (pn)
2020 Nov 22	0861250301	35.7 ks (RGS), 11.6 ks (pn)

SNe have been recorded in Arp 299 (Anderson et al. 2011). Six of them are identified as SNcc and one is unclassified (Anderson et al. 2011). According to the Open Supernova Catalog (Guillochon et al. 2017),[14] three more SNe have been found since 2010: SN2018lrd, SN2019lqo, and SN2020fkb. All three are SNcc. Nevertheless, due to the obscuration by large amounts of dust in Arp 299, Mattila et al. (2012) argue that ∼80% of the SNe are estimated to be missed by observations in the optical band.

Arp 299 hosts a hot atmosphere that dominates the soft X-ray spectrum below 2 keV (e.g., Anastasopoulou et al. 2016). About 20 ultraluminous X-ray sources (Zezas et al. 2003; Anastasopoulou et al. 2016) and at least one Compton-thick nucleus (Ptak et al. 2015) dominate the hard X-ray spectrum at 2–10 keV and >10 keV, respectively. Previous X-ray studies do not focus on accurate abundance measurement of O, Ne, and Mg, which are mainly enriched by SNcc. Here, we measure the elemental abundances of the hot atmosphere of Arp 299 with the high-quality X-ray spectra obtained with XMM-Newton. We compare the observed abundance ratios with various chemical enrichment models. These models include different SN yields, the initial mass functions (IMFs), the initial metallicities, and the mass ranges of the SNcc progenitors, and mixing fractions of HN or SNIa.

A supplementary package is available in the Zenodo repository at 10.5281/zenodo.5148020. This package includes data and scripts used to create the figures presented in this paper.

2. XMM-Newton Observations

We use all the X-ray spectra observed with XMM-Newton (Table 1), including three new observations obtained in Cycle 19 (PI: J. Mao). The data are reduced following the standard procedure using XMM-Newton Science Analysis Software (SAS) v19.0. We construct a time-averaged X-ray spectrum with the high-resolution soft X-ray spectra (7.5–27 Å) obtained with Reflection Grating Spectrometer (RGS; den Herder et al. 2001) and the relatively low-resolution hard X-ray spectra (1.6–10.5 Å) obtained with the positive–negative (pn) junction CCD (charge-coupled device) camera of the European Photon Imaging Camera (EPIC).

Lightcurves from the CCD9 of RGS and the 10–12 keV energy band of EPIC/pn are created with a time bin of 100 s. Time intervals contaminated by background soft-proton flares are identified as those above the 3σ level and excluded from the following data reduction. As shown in the left panel of Figure 1, we extract RGS spectra in rectangular regions centered on the source with the width along the cross-dispersion direction equal to ∼48″ (i.e., 90% of the point-spread function). We extract EPIC/pn spectra in a circular region with a radius of 24″. The RGS modeled background and pn local background spectra are subtracted. All the RGS spectra are combined, as well as the EPIC/pn spectra. By matching the flux in the common 7.5–10.5 Å wavelength range, the EPIC/pn spectra are scaled by 0.70 with respect to RGS to account for the different instrument normalization and the different aperture (the left panel of Figure 1). The right panel of Figure 1 shows a true color image of Arp 299. The soft X-ray (0.3–2 keV) image (in purple) is created with the XMM-Newton *image*[15] script. The optical image (in green) is taken with the Advanced Camera for Surveys Wide Field Channel (F814W filter, 814 nm) aboard the Hubble Space Telescope. The infrared image (in red) is taken with the Infrared Array Camera (Channel 1, 3.6 μm) aboard the Spitzer Space Telescope.

3. Spectral Analysis

For the spectral analysis, we use the SPEX code (Kaastra et al. 2020, v3.06.00), which includes the most recent atomic data for the Fe-L complex (Gu et al. 2020). We use *C*-statistics (Kaastra 2017), and statistical uncertainties are quoted at the 68% confidence level. With $H_0 = 70\ \mathrm{km\ s^{-1}\ Mpc^{-1}}$, $\Omega_M = 0.3$, and $\Omega_\Lambda = 0.7$, the redshift of the target is 0.0112 and a distance scale of $12.7\ \mathrm{kpc\ arcmin^{-1}}$.

The hot atmosphere is modeled with multi-temperature thermal plasma models. A power-law component (denoted as PL) is included to account for the point sources. Three Fe K lines with rest-frame energies of 6.4 keV, 6.7 keV, and 6.97 keV are also included. These Fe K lines are associated with the nucleus of NGC 3690, X-ray binaries, and supernova remnants (Ptak et al. 2015; Anastasopoulou et al. 2016). Since the power-law component dominates the flux above $\gtrsim$2 keV, the absolute abundance of the thermal plasma with respect to hydrogen cannot be well determined. We set the reference element to oxygen. The proto-solar abundance table of Lodders et al. (2009) is used.[16] Both the thermal and power-law components are corrected for absorptions of both the host galaxy and Milky Way. For the Galactic absorption, we use $N_{\mathrm{H}}^{\mathrm{MW}} = 9.35 \times 10^{19}\ \mathrm{cm^{-2}}$ (Willingale et al. 2013). Similar to Smith et al. (2018), we use different hydrogen column densities for the thermal and power-law components for the host galaxy absorption.

We ran a total of eight spectral fittings considering (1) various differential emission measure distributions, (2) mimicking the nonequilibrium scenario, (3) varying power-law photon indices, and (4) coupling the Fe and Ni abundances. Detailed results are presented in the Appendix. In Figure 2, we show the best-fit model to the observed X-ray spectrum of Arp 299. Most of the previous studies (Huo et al. 2004; Anastasopoulou et al. 2016; Smith et al. 2018) described the hot atmosphere as a single-temperature thermal (i.e., isothermal) component. Our best-fit results favor a multi-temperature description of the hot atmosphere. This should better reflect the multi-temperature nature of the hot atmospheres of starburst galaxies (Strickland & Stevens 2000).

[14] https://sne.space/

[15] https://www.cosmos.esa.int/web/xmm-newton/images

[16] The abundances denoted as X and X/O designate $(X/\mathrm{H})_{\mathrm{gas}}/(X/\mathrm{H})_{\odot}$ and $(X/\mathrm{O})_{\mathrm{gas}}/(X/\mathrm{O})_{\odot}$, respectively. They correspond to the ratios of X/H and X/O in the hot atmosphere to those in the proto-solar abundance table of Lodders et al. (2009).

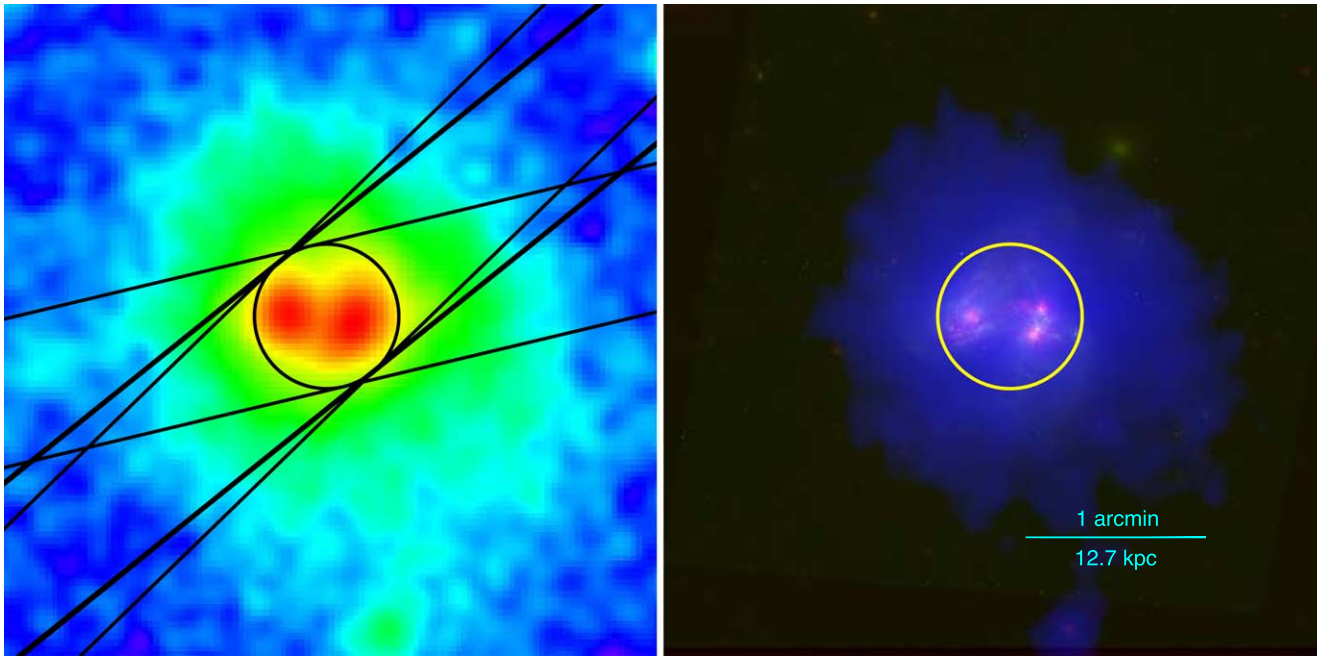

Figure 1. X-ray to IR image of Arp 299. Left: XMM-Newton soft X-ray (0.3–2 keV) image with the RGS (rectangles) and EPIC/pn (circle) source regions. The three new observations in 2020 (Table 1) have similar RGS roll angles so that one rectangular box appears thick. Right: the true color image of Arp 299 with soft X-ray in purple, optical (Hubble, 814 nm) in green, and infrared (Spitzer, 3.6 μm) in red.

4. Metal Abundances

Accurate abundance measurement of individual elements is essential to understand the chemical enrichment process of the hot atmosphere of Arp 299. In the present work, we measure the abundance ratios of $\mathrm{N/O} = 0.70^{+0.38}_{-0.29}$, $\mathrm{Ne/O} = 1.16 \pm 0.21$, $\mathrm{Mg/O} = 1.27 \pm 0.26$, $\mathrm{Si/O} = 0.97 \pm 0.23$, $\mathrm{S/O} = 1.78 \pm 0.57$, $\mathrm{Fe/O} = 0.40^{+0.06}_{-0.05}$, and $\mathrm{Ni/O} = 0.66^{+0.31}_{-0.27}$. Our measurement takes advantage of the resolving power of the RGS spectra for emission lines of N, O, and Fe-L. Previous studies either do not measure individual elements separately or only cover a few elements. Huo et al. (2004) measured merely the Fe abundance ($0.12^{+0.21}_{-0.05}$) of the thermal plasma model MEKAL (Mewe et al. 1995), which does not contain the state-of-the-art atomic data. Anastasopoulou et al. (2016) used VAPEC and measure the abundances of Ne ($1.24^{+0.34}_{-0.29}$), Mg ($1.14^{+0.25}_{-0.20}$), and Fe ($0.26^{+0.04}_{-0.03}$). Smith et al. (2018) used VMEKAL and measured merely the α/Fe ($= 3.25 \pm 2.48$) abundance ratio.

We also note that the abundance ratios measured in the X-ray band are more robust than the absolute abundance with respect to hydrogen, especially for relatively cool thermal plasmas with its weak bremsstrahlung (free–free) emission dominated by the power-law component of the host galaxy. The absolute oxygen abundance (O/H) of the H II regions that are closest to the seven SNe exploded in 1992–2010 ranges from $\sim$0.53 to $\sim$0.70 solar (Anderson et al. 2011). The absolute oxygen abundance (O/H) of the interstellar medium of NGC 3690 is $\sim$0.66 solar (Heckman et al. 2015).

In other well studied X-ray bright starburst galaxies, super-solar Ne/O and Mg/O have been reported. For NGC 253, the Mg/O and Ne/O abundance ratios are $\sim$2–3 times solar for the central and surrounding regions (Bauer et al. 2007). For M82, while the stellar abundances are almost solar, the hot atmosphere Mg/O and Ne/O abundance ratios are $\sim$2–5 times solar (Origlia et al. 2004). After taking into account the charge exchange effect (Zhang et al. 2014), these two abundance ratios are still about twice solar with $\mathrm{Ne/O} = 2.2 \pm 0.3$ and $\mathrm{Mg/O} = 2.1 \pm 0.3$, respectively.

5. Metal Enrichment via Supernovae

To interpret the observed abundance ratios, we build a simplified chemical enrichment model based on SNcc and SNIa nucleosynthesis yields. SNIa is included here to take into account the potential contribution of a "prompt" population of SNIa (Maoz et al. 2014) that explode within a few hundreds of million years after the peak star formation activity. The theoretical abundance ratios are calculated via

$$\frac{z_i}{z_j} = \frac{\bar{y}_i^{\mathrm{SNcc}} + r^{\mathrm{SNIa}}\, y_i^{\mathrm{SNIa}}}{\bar{y}_j^{\mathrm{SNcc}} + r^{\mathrm{SNIa}}\, y_{\mathrm{j}}^{\mathrm{SNIa}}} \frac{A_j\, n_j}{A_i\, n_i}, \quad (1)$$

where $z_{i,j}$ are the abundance of the ith or jth element, y_i^{SNcc} the IMF-weighted SNcc yields, r^{SNIa} the number ratio of SNIa with respect to SNcc, y_i^{SNIa} the SNIa yields, $A_{i,j}$ the atomic weight of the ith or jth element and $n_{i,j}$ are the elemental abundance by number in the (proto-)solar abundance table.

We do not have accurate abundances of Fe-peak abundances (e.g., Cr, Mn, and Ni) other than Fe. Therefore, we cannot break degeneracy of dozens of SNIa yields available in the literature. For simplicity, we adopt the widely used W7 yields of Iwamoto et al. (1999) when investigating the contribution from a "prompt" population of SNIa.

The IMF weighted SNcc yields[17] are calculated via:

$$\bar{y}_i^{\mathrm{SNcc}} = \frac{\int_{m_{\mathrm{lo}}}^{m_{\mathrm{up}}} \phi(m)\, y_i(m)\, dm}{\int_{m_{\mathrm{lo}}}^{m_{\mathrm{up}}} \phi(m)\, dm}, \quad (2)$$

[17] Only single-star SN nucleosynthesis yields are considered here.

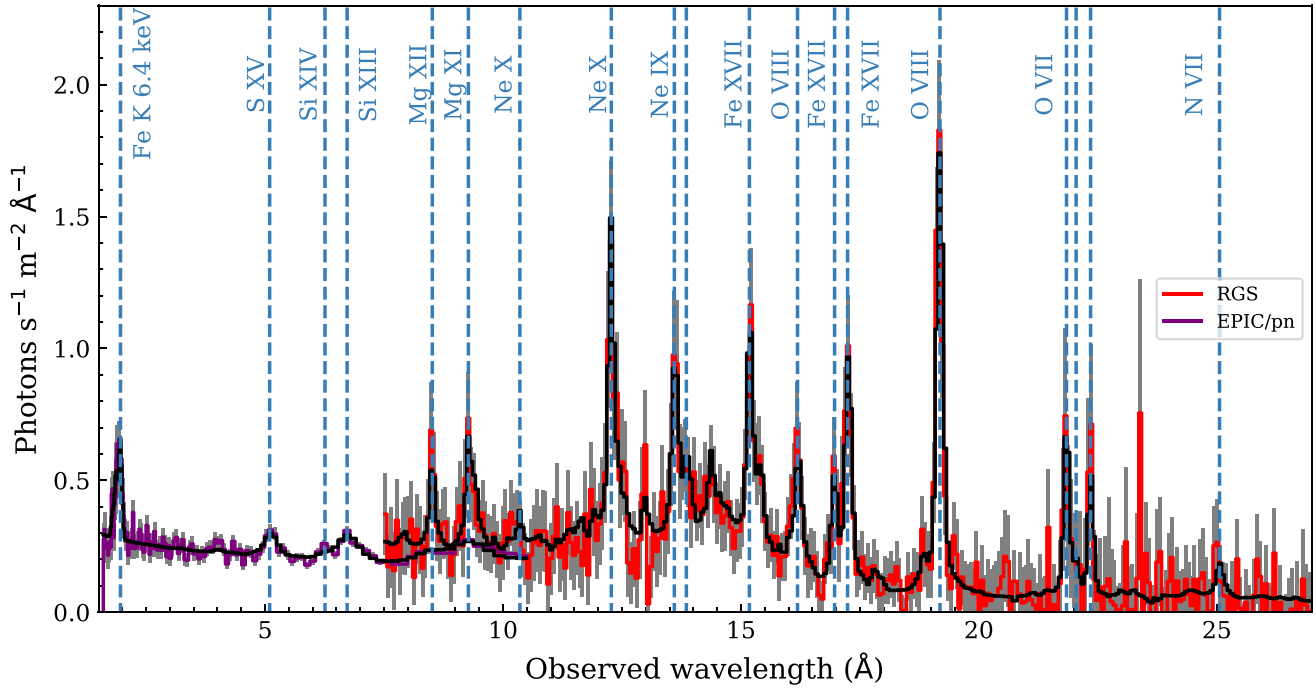

Figure 2. The best-fit model (Model M4 in Table 2) to the X-ray spectrum of Arp 299 observed with XMM-Newton. The high-resolution RGS spectrum is shown in red, while the EPIC/pn spectrum is shown in purple. The 1σ uncertainties are shown in gray. The RGS spectrum is rebinned here for clarity. Vertical dashed lines in blue mark key diagnostics emission lines in the spectrum.

where $\phi(m) \propto m^{\Gamma}$ is the IMF, and $m_{\rm lo}$ and $m_{\rm up}$ are the lower and upper mass limits of the progenitors, which depend on the initial metallicity. The Salpeter IMF (Salpeter 1955, $\Gamma = -2.35$) is adopted here as the default. SNcc yields are sourced from Nomoto et al. (2013) and Sukhbold et al. (2016). Nomoto et al. (2013, N13) provide SNcc yields of massive stars with different initial metallicities ($Z = 0$, 0.001, 0.004, 0.008, 0.02, and 0.05). The mass ranges of the progenitor are 11–140 $M_{\odot}$ for $Z = 0$ and 13–40 $M_{\odot}$ for $Z > 0$. Taking advantage of a one-dimensional neutrino transport model for the explosion, Sukhbold et al. (2016, S16) provide SNcc yields of massive (12.25–120 $M_{\odot}$) stars with solar metallicity ($Z = 0.02$). Both the W18 and N20 models of Sukhbold et al. (2016) are considered here. The former was calibrated so that a Nomoto & Hashimoto (1988) progenitor explodes like SN 1987A, while the latter was calibrated so that a Utrobin et al. (2015) progenitor explodes like SN 1987A.

As shown in Figure 3, the calculated IMF weighted abundance ratios are not within the $\gtrsim 1\sigma$ uncertainties of the observed ones. The closest match is the one with N13 yields for massive (13–40 $M_{\odot}$) stars with solar metallicity ($Z = 0.02$). In the following, we tried to vary several underlying parameters based on the N13 $Z = 0.02$ model.

First, we tried to vary the IMF power-law index. For Arp 299, the relatively high frequency of "stripped-envelope" SNe (type Ib and type IIb) with respect to normal type II SNe suggests that the IMF of the host galaxy is biased toward the production of high-mass stars (Anderson et al. 2011).[18] In Figure 3, the purple filled circles illustrate the effect of varying the IMF power-law index. A top-heavy IMF with $\Gamma = -2.0$ can decrease the abundance ratios (X/O) by $\lesssim 0.06$, while a bottom-heavy IMF with $\Gamma = -2.7$ can increase the abundance ratios (X/O) by $\lesssim 0.06$. Both cases do not improve the mismatch.

Varying the upper mass limit of the massive progenitors can bring the calculated abundance ratios closer to the observed ones. The blue curve and filled circles in Figure 3 illustrate the effect of varying $m_{\rm up}$ in Equation (2). The observed abundance ratios N/O, Ne/O, Mg/O, S/O, and Ni/O can be better explained if massive progenitors up to ~23–27 $M_{\odot}$ explode as SNcc and enrich the hot atmosphere with metals. The Si/O–Mg/O and Fe/O–Mg/O patterns favor $m_{\rm up} \gtrsim 30\,M_{\odot}$ with the observed Mg/O ratio larger than the theoretical ones. If the theoretical SNcc nucleosynthesis yields of Mg/O yields are underestimated (Griffith et al. 2021), say by 20%, a more consistent match might be found for all six abundance patterns. In this case, the upper limit of the SNcc progenitors can be larger than ~23–27 $M_{\odot}$.

We further consider a more complicated scenario where massive progenitors with $M_{\star} \sim 13$–$20\,M_{\odot}$ explode as SNcc while a fraction of massive progenitors with $M_{\star} \sim 20$–$40\,M_{\odot}$ explode as HN.[19] The pink curve and filled circles in Figure 3 illustrate this mixing effect. The abundance pattern of Ne/O–Mg/O can break the degeneracy between the HN fraction and $m_{\rm up}$ cutoff. Taking into account that SNcc are the dominant metal factory of O, Ne, and Mg (i.e., contributions from AGBs and SNIa are negligible), the Ne/O–Mg/O pattern is the best one to explore the difference of theoretical chemical enrichment models of SNcc.

We also consider an alternative complicated scenario where massive progenitors with a mixture of SNcc (from massive stars with $M_{\star} \sim 13$–$40\,M_{\odot}$) and SNIa. Here we consider the number of SNIa to that of SNcc ($r_{\rm SNIa}$ in Equation (2)) ranges

[18] Note that "stripped-envelope" SNe can also be produced by binary stars with a less massive progenitor (Smartt 2009).

[19] Nomoto et al. (2013) HN yields are available for $M_{\star} = 20$, 25, 30, and 40 $M_{\odot}$ with solar metallicity.

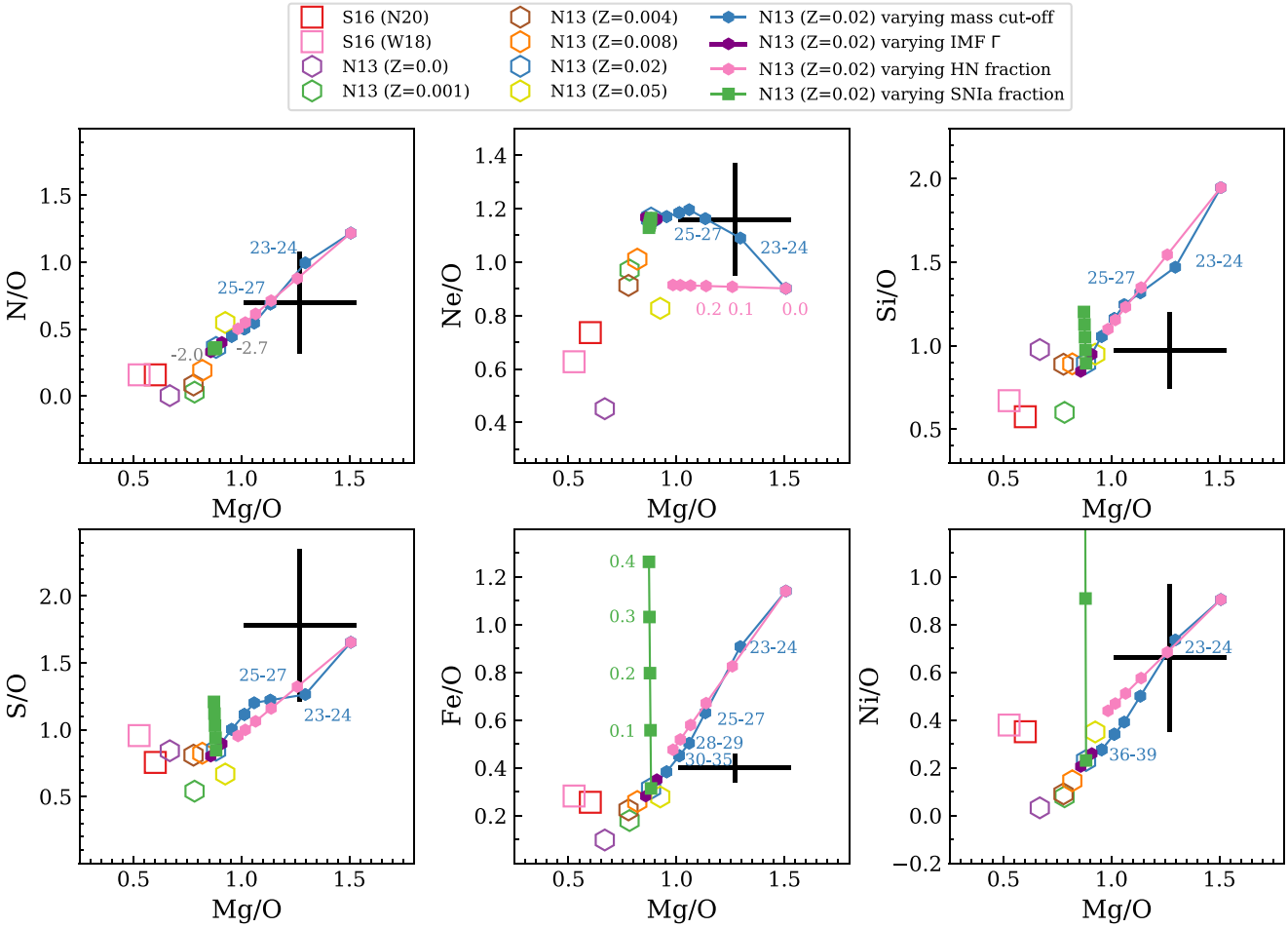

Figure 3. Elemental abundance patterns of the hot atmosphere of Arp 299. The observed abundance ratios (with 1σ uncertainties) are shown as black crosses. Chemical enrichment models with core-collapse supernovae (SNcc) yields from Sukhbold et al. (2016, S16) and Nomoto et al. (2013, N13) are shown as squares and hexagons, respectively. For the N13 models, we further consider different IMF power-law indices -2.0 (left) and -2.7 (right); different cutoff masses for the SNcc progenitors with the upper mass limits $M_{\rm up}$: 36–39 $M_\odot$ (leftmost), 30–35 $M_\odot$, 28–29 $M_\odot$, 25–27 $M_\odot$, 23–24 $M_\odot$, and 20–22 $M_\odot$ (rightmost); different hypernova fractions from 0.5 (leftmost) to 0.0 (rightmost) for massive stars with $M_\star \sim$ 20–40 $M_\odot$ (and SNcc for stars with $M_\star \sim$ 13–20 $M_\odot$); and different SNIa fractions from 0.0 (bottom) to 0.4 (top).

from 0.0 to 0.4. The green curve and filled squares in Figure 3 illustrate this mixing effect. The abundance patterns of N/O–Mg/O and Ne/O–Mg/O are barely affected by the SNIa fraction. As shown in Mernier et al. (2016), Simionescu et al. (2019), and Mao et al. (2019), even for rather old systems like elliptical galaxies, groups, and clusters of galaxies, where a significant fraction of SNIa has contributed to the chemical enrichment process, SNcc is still the dominant metal factory of O, Ne, and Mg. For heavier elements including Si, the increasing SNIa fraction will increase the abundance ratios to O.

In short, we find a hint of deviation between the observed abundance patterns and theoretical ones from a simple chemical enrichment model. The deviation can be explained if massive stars with $M_\star \gtrsim$ 23–27 $M_\odot$ do not explode as SNcc. This is in accordance with the missing massive SNcc progenitors problem, where SNcc observed so far are not produced by massive stars with $M_\star \gtrsim 18\,M_\odot$ (Smartt 2015). It is also possible that theoretical SNcc nucleosynthesis yields of Mg/O yields are underestimated (Griffith et al. 2021). Statistical uncertainties of the current data are still large, which can be significantly improved with the next generation of X-ray spectrometer like XRISM/Resolve (XRISM Science Team 2020) and Athena/X-IFU (Barret et al. 2018). Last but not least, we caution that the observed abundance ratios might not be directly compared to our simple chemical enrichment models. The metals produced by SNcc are distributed not only in the X-ray emitting hot atmosphere but also in the cooler phase of the interstellar medium (gas and dust). Inflows and outflows can further complicate the distribution and dilution of the metals.

We thank the referee for the careful reading of the manuscript and useful suggestions to improve the quality of this work. This work is based on observations obtained with XMM-Newton, anESA science mission with instruments and contributions directlyfunded by ESA Member States and NASA. J.M. acknowledges useful discussions with Jiangtao Li and H. Yamaguchi. P.Z. acknowledges the support from NSFC grant 11590781. A.S. is supported by the Women In Science Excel (WISE) program of the Netherlands Organisation for Scientific Research (NWO), and acknowledges the World Premier Research Center Initiative (WPI) and the Kavli IPMU for the continued hospitality. Y.S. acknowledges support from Chandra Grants AR8-19020A and GO1-22126X. SRON

Table 2
Best-fit Parameters and Statistics

Model	S	T	M1	M2	M3	M4	M5	M6
				Hot Atmosphere				
$N_{\rm H}^{\rm HA}$ (10^{21} cm^{-2})	0.9	1.2	1.3	1.5	1.7	$1.6^{+0.5}_{-0.3}$	1.6	1.5
$N_{\rm hot}$ (10^{64} cm^{-3})	1.7	1.5	2.1	2.2	2.4	$2.4^{+0.8}_{-0.5}$	2.4	2.3
$T_{\rm hot}$	0.59	0.62	0.61	0.67	0.66	0.67 ± 0.04	0.68	0.68
$\sigma_{\rm hot}(\log T)$	⋯	⋯	0.50	0.33	0.35	0.31 ± 0.05	0.36	0.32
$v_{\rm RMS,hot}$	830	930	810	840	840	840 ± 60	830	840
$N_{\rm cool}$ (10^{64} cm^{-3})	⋯	0.3	⋯	0.8	3.3	$0.6^{+2.1}_{-0.3}$	0.9	0.9
$T_{\rm cool}$	⋯	0.18	⋯	0.11	0.086	0.12 ± 0.04	0.11	0.11
T_b/T_e(cool)	⋯	1.0 (f)	⋯	1.0 (f)	1.6	1.0 (f)	1.0 (f)	1.0 (f)
$v_{\rm RMS,cool}$	⋯	930 (c)	⋯	840 (c)	840 (c)	380^{+250}_{-190}	830 (c)	840 (c)
N/O	0.85	0.58	0.87	0.69	0.53	$0.70^{+0.38}_{-0.29}$	0.70	0.68
Ne/O	1.21	1.47	1.44	1.22	1.20	1.16 ± 0.21	1.20	1.21
Mg/O	1.00	1.21	1.81	1.36	1.35	1.27 ± 0.26	1.34	1.29
Si/O	1.07	1.17	1.42	1.04	1.02	0.97 ± 0.23	1.05	0.96
S/O	3.8	3.9	2.2	1.89	1.77	1.78 ± 0.57	1.84	1.73
Fe/O	0.24	0.31	0.53	0.42	0.42	$0.40^{+0.06}_{-0.05}$	0.43	0.41
Ni/O	0.97	1.06	1.28	0.73	0.80	$0.66^{+0.31}_{-0.27}$	0.64	0.41 (c)
				Point Sources				
$N_{\rm H}^{\rm PS}$ (10^{21} cm^{-2})	4.0	4.0	5.1	6.3	6.8	$6.7^{+3.2}_{-1.5}$	5.7	6.6
$N_{\rm PL}$(10^{49} ph s^{-1} keV^{-1})	7.87	7.85	7.17	8.09	7.43	7.48 ± 0.02	6.56	7.43
$\Gamma_{\rm PL}$	1.67 (f)	1.67 (f)	1.67 (f)	1.67 (f)	1.67 (f)	1.67 (f)	1.59	1.67 (f)
$N_{\rm 6.4keV}$(10^{47} ph s^{-1})	11.8	11.8	12.6	12.4	12.5	12.43 ± 0.14	12.1	12.5
$N_{\rm 6.7keV}$(10^{47} ph s^{-1})	7.1	7.1	7.2	7.3	7.3	7.3 ± 1.3	7.1	7.4
$N_{\rm 7.0keV}$(10^{47} ph s^{-1})	2.1	2.2	2.9	2.6	2.7	2.6 ± 1.1	2.4	2.7
				Statistics				
$C_{\rm stat}$ (total)	1420.0	1353.2	1311.5	1295.8	1294.6	1292.8	1294.6	1297.1
d.o.f. (total)	1080	1078	1079	1077	1076	1076	1076	1078
$C_{\rm stat}$ (RGS)	1268.4	1203.7	1171.7	1157.7	1156.7	1155.1	1158.0	1157.6
$C_{\rm stat}$ (pn)	151.6	149.4	139.8	138.1	137.9	137.7	136.6	139.5

Note. The hot atmosphere is modeled with either a single-temperature (Model S), two-temperature (Model T), or multi-temperature (Models M1−M6) differential emission measure plasma model. The power-law (PL) component and Fe K lines are required for the point sources. The expected *C*-statistics (Kaastra 2017) are 1135 ± 49 (total), 1010 (RGS), and 125 (pn). Statistical uncertainties at the 68% confidence level are provided for the best-fit (Model M4). Frozen and coupled parameters are shown as (f) and (c), respectively.

is supported financially by NWO, the Netherlands Organization for Scientific Research.

Facilities: XMM, HST, Spitzer.

Software: SPEX v3.06.00 (Kaastra et al. 2020).

Appendix
Spectral Models

A total of eight spectral fittings were performed in the present work. The first three sets (S, T, and M0) in Table 2 adopt different differential emission measure distributions for the hot atmosphere: single-temperature (Model S), two-temperature (Model T), and a multi-temperature (Model M1) model with a Gaussian (log-normal) differential emission measure (DEM) distribution (GDEM; de Plaa et al. 2006),

$$Y(x) = \frac{Y_0}{\sigma\sqrt{2\pi}} \exp\left(-\frac{(x - x_0)^2}{2\sigma^2}\right), \quad \text{(A1)}$$

where Y and Y_0 are the emission measures, $x = \log_{10} T$, $x_0 = \log_{10}(T_0)$, and T_0 is peak temperature of the DEM distribution in units of keV. The single-temperature (i.e., isothermal) model is nested in Equation (A1) with $\sigma = 0$. Both the multi-temperature and two-temperature DEM distributions yield significantly better statistics.

Adding another single-temperature cool component to Model M1 can further improve *C*-statistics by ~ -16 at the cost of 2 less degrees of freedom (Model M2). The main improvement comes from O VII. Setting $\sigma(\log T)$ of this cool component free does not improve the fit at all with $\sigma(\log T)$ remains at zero. With still some residuals for the O VII lines, we set the temperature ratio T_b/T_e for the cool component (Model M3). For collisionally ionized equilibrium plasmas, the ionization balance temperature T_b equals the electron temperature T_e. A nonunity value can mimic nonequilibrium plasmas. For Model M3, we obtain $T_b/T_e \sim 1.6$, where the forbidden to resonant line ratio of He-like O VII triplet was boosted to better match the observed data. But *C*-statistics is merely improved by ~ -0.8 with one less degree of freedom. This indicates a minor contribution from nonequilibrium plasmas. The charge exchange process can also increase the the forbidden to resonant line ratio of He-like O VII triplet, as in M82 (Zhang et al. 2014). Considering the availability of H I and molecular gas in Arp 299 (e.g., Heckman et al. 1999; Sliwa et al. 2012), it is possible that charge exchange between the hot and cold gas plays a role here. Unfortunately, the quality of the current data

set is not sufficient to constrain the free parameters of the possible charge exchange process, such as the interacting atomic or molecular species, collision velocities, and different capture mechanisms to the *l*-subshells. In addition, based on Model M2, we decouple the turbulence velocity ($v_{\rm RMS}$) of the two thermal components in Model M4. This yields the best *C*-statistics among all eight models.

For all previous models (S to M4), the photon index of the power-law component was fixed to 1.67 as measured by Anastasopoulou et al. (2016) with joint Chandra and NuSTAR observations. In Model M5, we set the photon index free, which yields $\Gamma \sim 1.59$ but *C*-statistics is merely improved by ~ -0.8 with one less degree of freedom (compared to Model M2).

Last but not least, based on Model M2, we couple the Ni and Fe abundances in Model M6. This is driven by the imperfect Ni-L complex atomic data in SPEX v3.06.00. The best-fit results of Models M2 to M6 also provide an estimate of the systematic uncertainties, which are smaller than the statistical uncertainties of the current data. That is to say, the key abundance ratios (Ne/O, Mg/O, and Fe/O) do not vary significantly in these models.

ORCID iDs

Junjie Mao https://orcid.org/0000-0001-7557-9713
Ping Zhou https://orcid.org/0000-0002-5683-822X
Aurora Simionescu https://orcid.org/0000-0002-9714-3862
Yasushi Fukazawa https://orcid.org/0000-0002-0921-8837
Liyi Gu https://orcid.org/0000-0001-9911-7038
François Mernier https://orcid.org/0000-0002-7031-4772

References

Alonso-Herrero, A., García-Marín, M., Monreal-Ibero, A., et al. 2009, A&A, 506, 1541
Anastasopoulou, K., Zezas, A., Ballo, L., & Della Ceca, R. 2016, MNRAS, 460, 3570
Anderson, J. P., Habergham, S. M., & James, P. A. 2011, MNRAS, 416, 567
Barret, D., Lam Trong, T., den Herder, J.-W., et al. 2018, Proc. SPIE, 10699, 106991G
Bauer, M., Pietsch, W., Trinchieri, G., et al. 2007, A&A, 467, 979
de Plaa, J., Werner, N., Bleeker, J. A. M., et al. 2007, A&A, 465, 345
de Plaa, J., Werner, N., Bykov, A. M., et al. 2006, A&A, 452, 397
den Herder, J. W., Brinkman, A. C., Kahn, S. M., et al. 2001, A&A, 365, L7
Griffith, E. J., Sukhbold, T., Weinberg, D. H., et al. 2021, arXiv:2103.09837
Gu, L., Shah, C., Mao, J., et al. 2020, A&A, 641, A93
Guillochon, J., Parrent, J., Kelley, L. Z., & Margutti, R. 2017, ApJ, 835, 64
Heckman, T. M., Alexandroff, R. M., Borthakur, S., Overzier, R., & Leitherer, C. 2015, ApJ, 809, 147
Heckman, T. M., Armus, L., Weaver, K. A., & Wang, J. 1999, ApJ, 517, 130
Heger, A., Fryer, C. L., Woosley, S. E., Langer, N., & Hartmann, D. H. 2003, ApJ, 591, 288
Hitomi Collaboration, Aharonian, F., Akamatsu, H., et al. 2017, Natur, 551, 478
Huo, Z. Y., Xia, X. Y., Xue, S. J., Mao, S., & Deng, Z. G. 2004, ApJ, 611, 208
Iwamoto, K., Brachwitz, F., Nomoto, K., et al. 1999, ApJS, 125, 439
James, B. L., Aloisi, A., Heckman, T., Sohn, S. T., & Wolfe, M. A. 2014, ApJ, 795, 109
Kaastra, J. S. 2017, A&A, 605, A51
Kaastra, J. S., Raassen, A. J. J., de Plaa, J., & Gu, L. 2020, SPEX X-ray Spectral Fitting Package, v3.06.00, Zenodo, doi:10.5281/zenodo.3939056
Kobayashi, C., Umeda, H., Nomoto, K., Tominaga, N., & Ohkubo, T. 2006, ApJ, 653, 1145
Lodders, K., Palme, H., & Gail, H. P. 2009, LanB, 4B, 712
Mao, J., de Plaa, J., Kaastra, J. S., et al. 2019, A&A, 621, A9
Maoz, D., Mannucci, F., & Nelemans, G. 2014, ARA&A, 52, 107
Mattila, S., Dahlen, T., Efstathiou, A., et al. 2012, ApJ, 756, 111
Mernier, F., Biffi, V., Yamaguchi, H., et al. 2018, SSRv, 214, 129
Mernier, F., de Plaa, J., Pinto, C., et al. 2016, A&A, 595, A126
Mewe, R., Kaastra, J. S., & Liedahl, D. A. 1995, Legacy, 6, 16
Nomoto, K., & Hashimoto, M. 1988, PhR, 163, 13
Nomoto, K., Kobayashi, C., & Tominaga, N. 2013, ARA&A, 51, 457
Origlia, L., Ranalli, P., Comastri, A., & Maiolino, R. 2004, ApJ, 606, 862
Pereira-Santaella, M., Alonso-Herrero, A., Santos-Lleo, M., et al. 2011, A&A, 535, A93
Ptak, A., Hornschemeier, A., Zezas, A., et al. 2015, ApJ, 800, 104
Salpeter, E. E. 1955, ApJ, 121, 161
Sanders, D. B., & Mirabel, I. F. 1996, ARA&A, 34, 749
Sanders, J. S., & Fabian, A. C. 2006, MNRAS, 371, 1483
Simionescu, A., Nakashima, S., Yamaguchi, H., et al. 2019, MNRAS, 483, 1701
Sliwa, K., Wilson, C. D., Petitpas, G. R., et al. 2012, ApJ, 753, 46
Smartt, S. J. 2009, ARA&A, 47, 63
Smartt, S. J. 2015, PASA, 32, e016
Smith, B. J., Campbell, K., Struck, C., et al. 2018, AJ, 155, 81
Strickland, D. K., & Stevens, I. R. 2000, MNRAS, 314, 511
Sukhbold, T., Ertl, T., Woosley, S. E., Brown, J. M., & Janka, H. T. 2016, ApJ, 821, 38
Utrobin, V. P., Wongwathanarat, A., Janka, H. T., & Müller, E. 2015, A&A, 581, A40
Werner, N., Böhringer, H., Kaastra, J. S., et al. 2006, A&A, 459, 353
Werner, N., McNamara, B. R., Churazov, E., & Scannapieco, E. 2019, SSRv, 215, 5
Willingale, R., Starling, R. L. C., Beardmore, A. P., Tanvir, N. R., & O'Brien, P. T. 2013, MNRAS, 431, 394
XRISM Science Team 2020, arXiv:2003.04962
Zezas, A., Ward, M. J., & Murray, S. S. 2003, ApJL, 594, L31
Zhang, S., Wang, Q. D., Ji, L., et al. 2014, ApJ, 794, 61
Zhou, P., & Vink, J. 2018, A&A, 615, A150